Analysis by Ripley's function of the correlations involved during failure in quasi-brittle materials: Experimental and numerical investigations at the mesoscale

Vincent Lefort, Gilles Pijaudier-Cabot, David Grégoire

Analysis by Ripley's function of the correlations involved during failure in quasi-brittle materials: experimental and numerical investigations at the mesoscale

Vincent Lefort, Gilles Pijaudier-Cabot, David Grégoire*

Université Pau & Pays Adour
Laboratoire des Fluides Complexes et leurs Réservoirs (LFC-R, UMR5150)
Campus Montaury, F64600 Anglet, France

Abstract

–

Accepted manuscript in *Engineering Fracture Mechanics*.
10.1016/j.engfracmech.2015.07.046.
The final publication is available at:
https://dx.doi.org/10.1016/j.engfracmech.2015.07.046

–

The degradation of quasi-brittle materials encompasses micro-cracks propagation, interaction and coalescence in order to form a macro-crack. These phenomena are located within the Fracture Process Zone (FPZ). This paper aims at providing a further insight in the description of the FPZ evolution with the help of statistical analysis of damage. The statistical analysis relies on the implementation of Ripley's functions, which have been developed in order to exhibit patterns in image analyses. It is shown how a correlation length may be extracted from the Ripley's function analysis. Comparisons between experimental and numerical evolutions of extracted correlation lengths are performed.

Keywords: Fracture, Quasi-brittle materials, Fracture Process Zone, Boundary effect, Mesoscale, Mesoscopic model, Experimental, Acoustic emission, Ripley's functions

*Corresponding author.
Email address: david.gregoire@univ-pau.fr
URL: http://lfc.univ-pau.fr / *P.* + 33 5 59 57 44 79 / *F.* +33 5 59 57 44 39

Nomenclature

$\mathbf{B}$ matrix, which links the global and the local coordinate systems
$\mathbf{D}$ material stiffness matrix
$\mathbf{D}_e$ elastic stiffness matrix
$\mathbf{K}$ secant stiffness matrix
A lattice element cross-section area
a_0 three-point bending beam pre-notch length
b three-point bending beam out-of-plane thickness
D three-point bending beam depth
d cell-size of the square grid for dissipated energy analyses
$D(i,j)$ euclidean distance between two points i and j
$d_{\min}$ minimum distance for acoustic transducers
e distance between point C and the lattice element segment
E, γ model parameters, which control Young's modulus and Poisson's ratio of the equivalent continuum
e_{ij} edge effect correction factor between two points i and j
f Kuhn-Tucker functional
f_t tensile strength
G_f meso-level fracture energy
H distance functional used in Ripley's analyses
h lattice element length
I lattice element second moment
i, j points
K Ripley's function
K^{ran} Ripley's function of a perfect randomly distributed set of points
L Ripley's residual function
l lattice element cross-section width
$L^{\text{disk}}(r,R)$ analytical approximation of the residual function of a distribution located in a unique disk of radius R
N total number of points
point C lattice material point
r, R_0, R radius
R^* optimum radius, which best fits the residual analytical function L^{disk}
r_{max} position of the maximum of the residual function $L(r)$, which is defined as the extracted correlation length

S surface of the analysis box
u, v, ϕ degrees of freedom of a node: two translations (u, v) and one rotation (ϕ)
u_c displacement jumps in the local coordinate system
u_e degrees of freedom in the global coordinate system
v_{CMOD} CMOD imposed velocity
w_f initial slope of the softening curve
w_{cn} crack opening

α orientation of the element in the global coordinate system
ΔD_d dissipated energy in a single lattice element
$\Delta\omega$ increment of damage parameter
κ normal strain history dependent variable
ω damage variable
$\overline{\sigma}$ effective stress vector
ϕ^d concrete aggregate diameter
ϕ^d_{min} minimum value of the explicitly described aggregate diameters
Π_{int} inner perimeter
ρ density of points
σ stress vector associated to each degrees of freedom
σ_n normal stress associated to u
σ_s shear stress associated to v
σ_ϕ stress associated to ϕ
ε strain vector associated to each degrees of freedom
ε_0, c and q model parameters
ε_n normal strain associated to u
ε_s shear strain associated to v
ε_ϕ strain associated to ϕ
ε_{eq} equivalent strain

$\mathcal{P}$ point distribution

CMOD Crack Mouth Opening Displacement
FPZ Fracture Process Zone
ITZ Interfacial Transition Zone

1. Introduction

Fracture of quasi-brittle materials such as concrete or rocks is characterized by a macro crack surrounded by a damage zone. At the tip of the macro crack and ahead lies the so-called Fracture Process Zone (FPZ) which is a region of the material undergoing distributed damage. The size of the FPZ in these heterogeneous materials is large enough to influence the mechanical behaviour of the structure significantly. It does not depend on the structural size, but it is rather controlled by the local heterogeneities in the material as well as by the geometry of the specimen and the stress conditions. Therefore, size effect, understood here as the dependence of the dimensionless nominal strength of a structure on its size, is observed (e.g. when geometrically similar structures are compared, see for example [1]).

Experimentally, this damage zone may be characterized with the help of several direct and indirect techniques. The localization of acoustic events that can be detected during crack propagation is one well established technique from which the FPZ can be visualized and characterized (e.g. [2], [3], [4], [5]). The acoustic events generated during micro-cracking are recorded and post-processed in order to localize them with the help of time-of-flight algorithms. Hence, this technique provides information on the entire crack propagation process composed of distributed micro cracking and further coalescence into a macro crack. Haidar and co-workers [6] used a model mortar material to observe the correlation among the width of the FPZ measured by acoustic emissions analysis, the parameters entering in the description of size effect, and the so-called internal length used in classical non-local constitutive relations.

As far as modeling is concerned, macroscale approaches (e.g. continuum-based models) and mesoscale models (e.g. discrete or lattice-based models) are available. The first one involves a characteristic length, which controls the size of the FPZ and is more suited for classical structural analyses. In recent continuum-based macroscale models (see e.g. [7, 8, 9] among others), however, it has been pointed out that this internal length is not constant during the fracture process and also that it is influenced by boundaries, which could be expected since experimental works on fracture in concrete underline the influence of boundaries on the fracture energy [10]. The second approach relies on a mesoscale description of the material and on an explicit description of the heterogeneities in the material. Therefore, this approach is better suited in order to achieve an in-depth comprehension of the degradation

processes involved during fracture. As opposed to the continuum macroscale approach, mesoscale models do not introduce a characteristic length to drive the failure process. The failure process is driven by the larger heterogeneities, which are explicitly represented in the meso-model. At the scale of a lattice element or a discrete element, softening is introduced as a local property. Note that continuum-based models may also be used at the mesoscale [11] by explicitly describing the heterogeneities and then may be also suited to achieve an in-depth comprehension of the degradation processes involved during fracture.

Grassl and co-workers [12] demonstrated that lattice-based mesoscale modeling was very efficient at describing not only size effect on the peak load, but also the entire load deflection response of bending beams. Four geometrically similar sizes and three different notch lengths were considered. The experimental data obtained by Grégoire et al. [1] could be quite accurately described, once the model parameters at the mesoscale level had been calibrated for one notch length. In addition, the authors used this model for studying the incremental distribution of the dissipated energy densities, and they were able to track the evolution of the fracture process zone in the structure, depending on the size of the beams and on the boundary conditions.

In addition, Grégoire and co-workers [5] demonstrated that this lattice-based mesoscale approach is also capable to capture the local failure process realistically. Three point bending experiments coupled with acoustic emission analyses provided global responses of the same bending beams and local data in the form of the distribution of the acoustic events and its evolution in the course of fracture. The experimental data obtained by Grégoire et al. [5], in term of energy dissipation maps and histograms of the distances between damage events, could be quite accurately described with the same set of model parameters. Particularly, the agreement between the distributions of the relative distances between damage events show that the mesoscale model depicts the fracture process zone and its evolution during failure in a very consistent way compared to acoustic emission data. Unfortunately, and contrary to the case of direct tension, these histograms cannot be interpreted easily because the effect of the strain gradient in bending beams cannot be easily separated from the interaction between damage events that may develop in the course of fracture.

The purpose of this paper is to provide a further insight in the description of failure with the help of statistical analyses of damage. The statistical

analysis relies on the implementation of Ripley's functions [13], which have been developed in order to exhibit patterns in image analyses.

This paper is organized as follows: section 2 shows how Ripley's function may be used in the context of damage mechanics to extract a correlation length between damage events. Section 3 recalls briefly the lattice model used in this paper. Section 4 presents the comparison between the evolution of extracted correlation length during mesoscale numerical simulations and experimental three point bending tests where damage events are localized by acoustic emission techniques. Finally, numerical investigations of correlation length evolutions upon failure are presented in section 5 for both direct tension and three point bending specimens. Results show that the computed correlation length is not constant during failure and significant differences may be observed depending on the type of loading applied to the same specimen.

2. Ripley's functions applied to damage mechanics

2.1. Ripley's K function description

Ripley's K function proposed in Ref. [13] is a tool for analyzing completely mapped spatial point process data, i.e. data on the locations of events [14]. Particularly, it is used to characterize the randomness in the spatial spreading of point distributions. It is of high interest in spatial ecology and has been used to characterize the development and spreading of different patterns, such as cell migration [13], tree [15] and plant [16] dissemination or disease spreading [17]. Recently, Tordesillas *et al.* [18] extended this pattern characterization method to non-biological system to analyze diffuse granular failure. In this paper, we will use the Ripley's K function to characterize the interactions and the correlations induced by damage localization in quasibrittle fracture. The Ripley's K function may be adapted to study one, two or three-dimensional spatial data, but most of the developments have been performed in 2D, which will also be the case hereafter. For a spatial point distribution, the Ripley's K function may be defined as the ratio between the density of events and the mean number of events within a distance r of any chosen event in the distribution:

$$\begin{aligned} K(r) &= \frac{1}{N\rho} \sum_{i \in \mathcal{P}} \sum_{j \in \mathcal{P}} e_{ij} H(i,j,r) \\ \text{and} \quad H(i,j,r) &= \begin{cases} 1 \text{ if } D(i,j) \leq r \\ 0 \text{ if } D(i,j) > r \end{cases} . \end{aligned} \tag{1}$$

In Eq. 1, N is the total number of points, ρ is the point density, $\mathcal{P}$ is the point distribution and $D(i,j)$ is the euclidean distance between two points i and j. e_{ij} is an edge effect correction factor, which is introduced to take into account that, for points located near the boundary of the study area, the real number of neighbors can be underestimated because some of them may be located outside of the study area or outside the specimen [19]. In 2D, the general expression of this edge effect correction factor is given by:

$$e_{ij} = \frac{\pi D(i,j)}{\Pi_{\text{int}}(i,j)} \geq 1. \tag{2}$$

In Eq. 2, $D(i,j)$ is the euclidean distance between two points i and j and $\Pi_{\text{int}}(i,j)$ is the inner perimeter corresponding to the part of the perimeter of the circle, centered at i with a radius of $D(i,j)$, which is included inside the study area. This edge effect correction factor depends on the shape of the study area. Typical edge effect correction factor expressions for a rectangular study area may be found in [19].

2.2. Randomness characterization

The Ripley's K^{ran} function of a perfect randomly distributed set of points is simply given by:

$$K^{\text{ran}}(r) = \pi r^2 \ . \tag{3}$$

In order to characterize the randomness of a distribution, the Ripley's K function is usually compared to this reference function K^{ran} by defining the residual function L as:

$$L(r) = \sqrt{\frac{K(r)}{\pi}} - \sqrt{\frac{K^{\text{ran}}(r)}{\pi}} = \sqrt{\frac{K(r)}{\pi}} - r \ . \tag{4}$$

Within this definition, and for a randomly distributed set of points, the residual function stays equal to zero. Thus, plotting the residual L for an arbitrary point distribution may characterize the distance of this distribution to a perfect random one and then characterize the randomness of the distribution. Applying this concept to a set of damage points may lead to characterize how these damage points localize upon failure and therefore characterize the correlations between these damage points, which are related to the internal length in a nonlocal continuum setting.

In order to illustrate the capability of the method to capture the randomness of a given point distribution, Fig. 1 and Fig. 2 present two different

artificial point distributions and the corresponding residual functions. For each analysis, we generate[1] 5 distributions of points, and we plot the envelope of the 5 resulting residual functions. Each distribution is included in an area of 100 mm by 100 mm.

[Figure 1 about here.]

The first distribution (denoted "A") consists in 100 points randomly distributed in the area. The second distribution (denoted "B") consists in 9 disks (diameter 20 mm, spacing 25 mm) containing 5, 10, 50, 100, 200 or 500 points.

For the distributions "A" (Fig. 1), there is a correct concordance with the analytical expression concerning a perfect random distribution.

[Figure 2 about here.]

For the distributions "B" (Fig. 2), the residual function presents several peaks. A positive value of the residual function means that the density of points within a distance r is greater than the density in the area. The first peak, located at $r = 12$ mm, is linked to the diameter of the disks. The second part of the curve, (between $r = 22$ mm et $r = 35$ mm), is linked to the spacing between the disks. Note that no edge effect correction is used in the analysis of distributions "B" since there are no points located outside the analysis area.

We also observe that the residual functions of the different distributions "B" are similar, while there are 100 times more points in the highest density distribution compared to the lowest density distribution. Ripley's functions are estimated considering a density ratio, and thus they do not depend on the total number of points.

2.3. Correlation length extraction

The residual function estimated for a distribution of points which is localized spatially presents different maxima (figure 2). The position of these maxima are directly linked to the geometry assumptions used for generating the distribution (see section 2.2).

[1]The random fields are generated based on the random number generation procedure given in [20].

Figure 3 presents a distribution of 20 points located in a unique disk of radius $R_0 = 10$ mm and the corresponding residual function L. The position of the maximum of the residual function $r_{\max} \approx 15.9$ mm does not correspond directly to the disk radius since it depends also on the height and the length of the analyze area. However, the analytical expression of the residual function L^{disk} of a distribution of events located in a disk of radius R may be approximated by equation 5. For a given residual function L of a distribution located in a unique disk, equation 6 provides the expression of the optimum radius R^*, which best fits the residual analytical function L^{disk}. This has been done for the distribution presented in Figure 3. One obtains $R^* \approx 9.57$ mm, which corresponds to an estimate of the disk radius with an error of less than 4.5% for this very coarse distribution.

$$L^{\text{disk}}(r,R) = \begin{cases} \sqrt{\frac{S}{\pi R^2}}(r - \frac{r^2}{4R}) - r & \text{for r } \leq 2R \\ \sqrt{\frac{S}{\pi}} - r & \text{for r } > 2R \end{cases} \tag{5}$$

$$R^* = \frac{1 - \sqrt{1 - 2r_{\max}\sqrt{\frac{\pi}{S}}}}{2\sqrt{\frac{\pi}{S}}} \tag{6}$$

where S is the surface of the analysis box ($S = 0.1 \times 0.1\ m^2$ in Figure 3) and $r_{\max}$ is the position of the maximum of the residual function.

[Figure 3 about here.]

For a given distribution of damage events with no particular shape, we define the maximum $r_{\max}$ of the residual function $L(r)$ as the correlation length of the distribution. Thereby, this correlation length may be extracted directly from the evolution of the residual function.

Note that according to this definition, the extracted correlation length depends on the size of the analysis area. This dependance is attenuated for large analysis area ($R^* \to \frac{r_{\max}}{2}$ when $S \to +\infty$ in Eq. 6). Thereafter, all Ripley's functions are estimated for a sufficiently large analysis area of a given constant size 400×400 mm and no edge effect correction is required.

3. Lattice model description

A 2D plane-stress lattice model is used to characterize the correlations involved during failure in quasi-brittle materials. Practically, the lattice model

is used to monitor an evolving population of damage events (a damage event corresponds to a lattice element undergoing damage during a load step), which is analyzed at each load step with the correlation length extraction method presented in part 2.3 and based on Ripley function applied to damage mechanics. This lattice model is based on the numerical framework proposed by Grassl and Jirasek [21]. It has been shown in previous study that this mesoscale approach is capable not only to provide consistent global responses (e.g. Force v.s. CMOD responses) [12, 5] but also to capture the local failure process realistically [5]. The numerical procedure is briefly presented in this section. The reader may refer to references [21, 12, 5] for further details.

The lattice is made of beam elements and idealizes the meso-structure of concrete as a set of three different components: *aggregates*, *matrix* and the *interface* between them. The following assumptions are used:

(i) Aggregates are described as circular inclusions. Aggregates with a diameter ϕ^d greater than a fixed diameter value $\phi^d_{\min}$ are described explicitly. Their size distribution follows the grading of the concrete mixture and their spatial location is given by a random distribution defined by the cumulative distribution function proposed in Ref. [21]. Aggregates overlapping is avoided.

(ii) Fine aggregates are not described. They are included in the matrix which is an equivalent homogeneous material (made of cement paste and fine aggregates). Disorder due to the heterogeneity of the matrix which contains small aggregates is still kept, however, in the form of a correlated random distribution of mechanical properties. The correlation length is independent from the fineness of the lattice and therefore provides lattice element size independent results [22].

(iii) The large aggregate are elastic. The matrix material follows an isotropic - scalar - damage model.

(iv) Each aggregate is surrounded by an interface of thickness equal to one lattice element length which is endowed with a special constitutive relation. This interface is meant to represent the Interfacial Transition Zone (ITZ) in concrete. Its constitutive model is similar to that of the matrix, with different constants since the ITZ is usually weaker than the matrix.

Once the largest aggregates have been placed randomly within the sample, the matrix is meshed by randomly locating nodes in the domain, such that

a minimum distance is enforced. The lattice elements result then from a Delaunay triangulation (solid lines in figure 4a) whereby the middle cross-sections of the lattice elements are the edges of the polygons of the dual Voronoi tesselation (dashed lines in figure 4a). By contrast, the nodes located on both sides of an interface are not randomly distributed, but placed at special location in a such way that the edges of the Voronoi polygons define the interface between the aggregates and mortar (figure 4b).

[Figure 4 about here.]

Each node has three degrees of freedom: two translations (u, v) and one rotation (ϕ) as depicted in figure 4d. In the global coordinate system, the degrees of freedom of nodes 1 and 2, noted $u_e = (u_1, v_1, \phi_1, u_2, v_2, \phi_2)^T$, are linked to the displacement jumps in the local coordinate system of point C, $u_c = (u_c, v_c, \phi_c)^T$ by the following relation:

$$u_c = \mathbf{B} u_e \tag{7}$$

where

$$\mathbf{B} = \begin{bmatrix} -\cos\alpha & -\sin\alpha & -e & \cos\alpha & \sin\alpha & e \\ \sin\alpha & -\cos\alpha & -h/2 & \cos\alpha & \sin\alpha & -h/2 \\ 0 & 0 & \sqrt{I/A} & 0 & 0 & -\sqrt{I/A} \end{bmatrix} \tag{8}$$

where A is the element cross-section area and I its second moment (see [12] for details).

Point C is located at the center of the middle cross-section of the element as represented in figures 4c and 4d. The matrix $\mathbf{B}$ depends on the orientation α of the element in the global coordinate system, the distance e between point C and the segment relating nodes 1 and 2, the distance h between two nodes, the element cross-sectional area A and its second moment I. The strains $\varepsilon = (\varepsilon_n, \varepsilon_s, \varepsilon_\phi)^T$ associated to the displacement u_c at point C are:

$$\varepsilon = \frac{u_c}{h} = (\varepsilon_n, \varepsilon_s, \varepsilon_\phi)^T \tag{9}$$

where h is the distance between the two nodes of one lattice element. The stresses $\sigma = (\sigma_n, \sigma_s, \sigma_\phi)^T$ are related to the strains ε following the mechanical constitutive relation at the lattice level, here an isotropic damage model to be described further. The subscripts n and s refer to the normal and shear components of the strain and stress vector. The (secant) stiffness matrix $\mathbf{K}$ of the lattice element is defined as follows:

$$\mathbf{K} = \frac{A}{h} \mathbf{B}^T \mathbf{D} \mathbf{B} \tag{10}$$

where $\mathbf{D}$ is the material stiffness matrix computed at point C.

The same isotropic damage model (Eq. 11) is used to describe the mechanical response of lattice element within the interfacial transition zone and the mechanical response of the matrix:

$$\sigma = (\sigma_n, \sigma_s, \sigma_\phi)^T = (1-\omega)\mathbf{D}_e\varepsilon = (1-\omega)\overline{\sigma} \tag{11}$$

where ω is the damage variable, $\mathbf{D}_e$ is the elastic stiffness and $\overline{\sigma} = (\bar{\sigma}_{\mathrm{n}}, \bar{\sigma}_{\mathrm{s}}, \bar{\sigma}_\phi)^T$ is the effective stress. The elastic stiffness

$$\mathbf{D}_{\mathrm{e}} = \begin{bmatrix} E & 0 & 0 \\ 0 & \gamma E & 0 \\ 0 & 0 & E \end{bmatrix} \tag{12}$$

depends on model parameters E and γ, which control Young's modulus and Poisson's ratio of the equivalent continuum [23]. Equations (8) and (12) were chosen so that for $h = \ell$ and $e = 0$ the stiffness matrix $\mathbf{K}$ reduces to the Bernoulli beam stiffness matrix ([24]).

The equivalent strain is then calculated from equation (13) where ε_0, c and q are model parameters.

$$\varepsilon_{eq} = \frac{1}{2}\varepsilon_0(1-c) + \sqrt{\left(\frac{1}{2}\varepsilon_0(c-1) + \varepsilon_n\right)^2 + \frac{c\gamma^2\varepsilon_s^2}{q}} \tag{13}$$

The expression for the damage parameter ω is derived by considering pure tension where the softening curve under monotonically increasing tensile strain is chosen to be of the exponential-type:

$$\sigma_n = f_t \exp\left(-\frac{w_{cn}}{w_f}\right) \tag{14}$$

where $w_{cn} = \omega h \varepsilon_n$ is the crack opening, w_f is the initial slope of the softening curve, which is related to the meso-level fracture energy as $G_f = f_t w_f$. This stress-strain law can also be written, for pure traction, as a function of the damage variable as in equation (15).

$$\sigma_n = (1-\omega)E\varepsilon_n \tag{15}$$

In pure tension, the nominal stress is limited by the tensile strength ($f_t = E\varepsilon_0$) and thus, by using these two expressions of σ_n, (14) and (15), one obtains the expression which governs the evolution of the damage variable ω:

$$(1-\omega)\kappa = \varepsilon_0 \exp\left(-\frac{\omega h \kappa}{w_f}\right) \tag{16}$$

where ε_n has been replaced by κ which is a history dependent variable determined by Eq. (17a) with the Kuhn-Tucker loading-unloading conditions (17b):

$$f(\varepsilon, \kappa) = \varepsilon_{eq}(\varepsilon) - \kappa \tag{17a}$$

$$f \leq 0, \quad \dot{\kappa} \geq 0, \quad \dot{\kappa} f = 0 \tag{17b}$$

The elastic constants and the model parameters in the damage models are calibrated from an inverse analysis technique. The material constants defining the mechanical behaviour of the three material components are usually calibrated assuming certain ratios of their respective mechanical properties. The interfacial transition zone (ITZ) has a smaller tensile strength and a smaller fracture energy compared to the matrix. Typically it has half the strength and half the fracture energy of mortar in the calculations. Experimental results for these ratios are reported in the literature (e.g. [25, 26]).

4. Model validation by experimental comparisons of correlation length evolutions

Three-point bending tests were performed on geometrically similar notched and unnotched specimens made of the same concrete material. The experimental results presented hereafter are obtained from a campaign already presented by Grégoire *et al.* [5]. This campaign is similar to the one previously presented by Grégoire *et al.* [1] and includes the localisation of acoustic events during fracture additionally. The experimental procedure is briefly presented in this section. The reader may refer to references [1, 5] for further details.

4.1. Experimental procedure: material, specimen and test rig descriptions

The concrete formulation used here is based on a ready-mix concrete mixture obtained from Unibeton (http://www.unibeton.fr) and detailed in table 1. Detailed gradings of the sand, the aggregates and the mix are given in [1].

[Table 1 about here.]

After demolding, the specimens were stored under water at 20°C. The characterization of their mechanical properties was made by compression and

splitting (Brazilian) tests according to European standards (EN 12390-1-3-6). Table 2 summarizes these mechanical properties. Since the concrete used for the present study is the same as the one used in [1, 5], detailed information about the mechanical response of the material is not repeated. The testing rig used for the bending tests was a three-point bending setup on a servo-hydraulic testing machine (HB250, Zwick/Roell) (see figure 5.a and figure 5.b).

[Table 2 about here.]

[Figure 5 about here.]

Figure 5.c presents a sketch of the specimen geometry and the different measurable quantities. Three HN200 half-notched specimens ($D = 200$ mm; $a_0 = 0.5D$), three FN200 fifth-notched ($D = 200$ mm; $a_0 = 0.2D$), two UN200 unnotched ($D = 200$ mm; $a_0 = 0$ mm) and three UN100 unnotched ($D = 100$ mm; $a_0 = 0$ mm) have been tested. The thickness was kept constant (50 mm). All tests were CMOD controlled at an imposed velocity (v_{CMOD}) in order to avoid post-peak unstable crack propagation. Table 3 summarizes the different specimen dimensions and the experimental conditions. The CMOD measurement was achieved by recording the distance between two aluminium plates glued on the bottom of the surface beam separated by the initial moulded notch. On the unnotched beams these metallic plates are glued at a distance equal to a half depth from the middle of the beam to ensure that the crack initiates between the two plates. In this case, the measure is not a CMOD. The numerical simulations were performed accordingly. Figure 6 gives a representation of the notched and unnotched beams and the corresponding positions of the aluminium plates. The CMOD was gradually increased until the complete failure of the structure.

[Table 3 about here.]

[Figure 6 about here.]

4.2. Acoustic Emission measurements

During the tests, acoustic events were recorded and localised. The AE system used in this study comprised an eigth-channel MISTRAS system, a general purpose interface bus (PCI-DISP4) and a PC for data storage analysis. Four acoustic transducers (resonant frequency of 150 kHz) were placed

around the expected location of the crack, on one side of specimen. The AE event localisation program relies on time of flight analysis and triangulation. The criterion used is that waves generated must reach at least 3 sensors. Then, the source location is determined by a 2D triangulation algorithm which relies of AEs arrival time and wave velocity. The details about AE setting parameters are given in [27]. Transducers were installed so that a minimum distance $d_{\min} = 1.25$ cm to the location where the crack could appear was respected in order to minimize errors which may occur when events are located near one sensor. Figure 7 shows the arrangement of the transducers for all the tested geometries.

[Figure 7 about here.]

The detected signals were then amplified with a 40dB gain differential amplifier in a frequency band from 20 to 120 kHz. In order to limit the background noise, the signal detection threshold was set at a value of 35 dB. The coupling between the transducer and the specimen is important in order to achieve a good accuracy of the localization of events. A thin layer of silicone grease was used to guarantee the correct transmission of acoustic signals between the beam and the transducer. The validation of both this coupling and the accuracy of the acoustic events localisation followed the European standard NF EN 1330. It consists in verifying if the position of an on-surface signal generated by the break of a short piece of pencil lead is correctly determined by the triangulation software. Thus, events were generated at several locations on the surface of each specimen and the results from the localisation software were compared with the true location of each event. A correct coupling is achieved when the accuracy of localization of these events is of the order of 4 mm.

Figure 8 shows the results of the cumulative locations of the acoustic events. The plotted points indicate the detected AE sources over the observation window centered at the notch. Events carry different energies and we have plotted here all the events. The warmer/darker the marker of one event, the higher the acoustic energy (color/black&white). One can filter the events and retain only those with a sufficiently large acoustic energy. These events should correspond to the macrocrack propagating in the specimen. Such an analysis points out that the process begins with low energy events distributed in a diffuse way, followed by a concentration of events with an increased rate of dissipated energy (see also [2]). For notched specimens, the inception and the path of the macro-crack is characterized by a strong

concentration and by alignment of the most energetic events. For unnotched specimens, acoustic events are spread on the bottom of the beam prior to the propagation of a single macrocrack on which the most energetic events are recorded. The location of crack initiation results from a competitive effect between the strain gradient and the local distribution of weak defects.

[Figure 8 about here.]

4.3. Numerical simulations: geometry, model parameter and global mechanical responses

Figures 9 and 9 present a schematic drawing of the notched and unnotched beams considered in the present study. The geometry and applied loads correspond to the experiments reported in Refs. [1, 5] and modeled numerically in Refs. [12, 5]. Four different sizes of geometrically similar specimens were considered, along with three notch lengths: $a_0 = 0$ (UnNotched, so-called UN), $a_0 = 0.2D$ (Fifth-Notched, so-called FN) and $a_0 = 0.5D$ (Half-Notched, so-called HN). For a detailed presentation of the experiments, see [1, 5].

The analyses were controlled by the crack mouth opening displacement (CMOD), which is the relative horizontal displacement of the points A and B shown in Figures 9 and 9. For the notched specimens, the points were located at the end of the notch. For the unnotched specimen, the two points were apart a distance equal to the beam depth D, since the location of the fracture process zone initiating from the surface was indeterminate.

Same as in the experiments, the out-of-plane thickness was kept constant for all sizes and all geometries at $b = 50$ mm. The notch thickness was fixed equal to zero for consistence with the experimental procedure where the notch was moulded using a thin metal plate of constant thickness. The load and support reactions were applied by means of 5 mm-wide metallic plates.

[Figure 9 about here.]

In order to limit the computation time, the nonlinear mesoscale model is used in the middle part of each beam centered at mid-span where damage is expected, as shown in Figures 9 and 9. The remaining part of the beam is discretized with elastic lattice elements. In this region, the aggregates are not described explicitly. The mechanical response of this part of the lattice

corresponds to that of the equivalent homogeneous material. The aggregate volume fraction corresponds to the experimental data[2], with a cut off for small sizes: $\phi^d_{\min} = 5$ mm. Fine aggregates are not explicitly described. They are included in the matrix which is an equivalent homogeneous material made of cement paste and fine aggregates. Disorder due to the heterogeneity of the matrix is considered in the form of a correlated random distribution of mechanical properties. The correlation length is equal to 1 mm. Details may be found in [12]. The model parameters for the three components are summarized in table 4. Such as in Ref. [12], these values were chosen so that the global model results in term of load-CMOD curves for different beam sizes and boundary conditions were in agreement with experimental results reported in [5]. However, not all parameters were varied independently of each other to obtain this agreement. Instead, several constraints were applied, motivated by experimental and numerical results reported in the literature. Firstly, the ratio of the stiffnesses for aggregate and matrix was kept constant and equal to two. Furthermore, the tensile strength of matrix was assumed to be twice of the strength of the interfacial transition. These ratios are in the range of the experimental results reported in [25, 26]. Furthermore, the model parameters for the elastic response outside the meso-scale region were chosen so that the response represents the average elastic behaviour of the meso-scale region.

[Table 4 about here.]

For each geometry, calculations were repeated with 10 different random fields of aggregates and mechanical properties.

The experimental and numerical results in term of Force vs. CMOD data are presented in Figure 10. As already discussed in [5], the experimental datapoints are in good agreement with the results obtained via the mesoscopic approach.

[Figure 10 about here.]

4.4. Comparison in term of correlation length evolutions

In this section, we aim at comparing the experimental data and the numerical results in term of evolutions of the correlation length extracted based

[2]The concrete mixture formulation is detailed in Table 1. Experimental data and detailed gradings of the sand, the aggregates and the mix are given in [1].

on the analysis by Ripley's functions and the procedure presented in section 2.3. To perform the comparison between the experimental and the numerical results, different statements have to be considered:

- **Damage event definition.**
  The procedure of correlation length extraction presented in section 2.3 is based on the analysis by Ripley's function of a given distribution of damage events. Experimentally, a damage event is associated to a material point producing acoustic emissions upon failure, which have been detected and then localized by at least three acoustic sensors during a load step. Numerically, a damage event is associated to a lattice material point (Point C in figure 4.d) undergoing damage during a load step.

- **Loading curve discretization.**
  A minimum number of damage events has to be captured to perform the post-processing. Numerically there is almost no limitation because a lot of damage events are acquired within a loading step. Experimentally, the acoustic emission is much more restrictive because only few acoustic events may be acquired by the technique, especially in the nonlinear pre-peak regime. Therefore, the loading curve discretization is determined to ensure to capture enough events experimentally in order to achieve a statistically representative post-processing. Since the first goal of this section is to test the relevance of the meso-model by comparing the numerical results with experimental ones, we adopt the same interval length, which is driven by the experimental minimum. Numerical investigations on correlation length evolutions upon failure based on a finer loading curve discretization are presented alone in part 5.

- **Space discretization.**
  Numerically, the space discretization corresponds intrinsically to the lattice discretization. Experimentally, there is an implicit space discretization due to the acoustic sensor resolution and the acoustic emission localization technique resolution. This resolution is of the order of 4 mm [5]. This means that two acoustic emissions produced at two different material points separated by a distance smaller than this resolution may not be distinguished. This means also that all the acoustic emissions produced in the corresponding vicinity of a material point are

seen by the acoustic sensors as a single acoustic emission with an acoustic energy corresponding to the addition of all the individual acoustic energies. Therefore the numerical and experimental data cannot be directly compared since the Ripley's function post-processing is only based on the spatial repartition of a given distribution of point. Experimentally, an acoustic event will count for a single data point in the Ripley's function analysis even if, locally, several material points undergo damage and produce acoustic emissions. This is overcome by tacking into account the intensity of the energy dissipated during each damage event in the post-processing by Ripley's functions. Assuming that the acoustic energy recorded for each event is proportional to the energy dissipated during the corresponding damage event, it is possible to compare experimental and numerical results in term of dissipated energy:

- On one hand, the dissipated energy during damage is obtained numerically from the mesoscale analysis. Maps of dissipated energy have been already computed in [21, 12, 5] and we follow the same procedure. The domain to be analyzed is first discretized with a square grid with a cell-size $d = 5$ mm. Within each cell, the energy dissipation due to damage is computed for each lattice element located in the cell. The dissipated energy in a single lattice element is calculated as $\Delta D_d = \Delta\omega A h \frac{1}{2}\varepsilon D\varepsilon$. Here $\Delta\omega$ is the increment of damage parameter; h, A, ε and D were defined in section 3. Then, we sum this energy dissipation for all lattice elements contained in the cell. When a lattice element crosses several cells, the energy is allocated in proportion to the element length within each cell.
- On the other hand, the maps of the distribution of acoustic energy within the same loading increments are computed according to the same discretization. Within an increment, the energy of all the event contained in the same cell is summed up. Due to the localization resolution by acoustic emission technique, less acoustic events than numerical events are detected. Therefore, the size and the discretization of the load increments are determined to ensure to capture enough events experimentally in order to achieve statistically representative post-processing.

Finally, the experimental and numerical energies dissipated within each cell are converted proportionally into a number of points, which are randomly spreaded within the cell. Since the Ripley's function post-processing does not depend on the total number of points (see figure 2), the post-processing does not depend on this proportionality factor. Practically, the maximum value of the energy (numerical dissipated energy or experimental acoustic energy) is converted into 200 points. After conversion, experimental and numerical evolutions of extracted correlation length may be compared. Note that after conversion, the extracted correlation lengths are smaller than the one extracted without any conversion and they are not directly linked to the fracture process zone size or to the internal length in the sense of nonlocal models because a large number of points are artificially placed close to the macro-crack path corresponding to high energy events. This is acceptable in this section where the first goal is to compare experimental and numerical data. Numerical investigations on correlation length evolutions upon failure without any conversion are presented alone in part 5.

Figure 11 presents the comparison between experimental and numerical extracted correlation length with intensity conversion. The correlation length is extracted based on the analysis by Ripley's functions as presented in section 2.3. Even if an important scattering is observed on the experimental data, we observe a global good agreement between the experimental and the numerical results. This means that the numerical model and the Ripley's post-processing procedure may be used alone to investigate the evolution of the correlation length upon failure.

[Figure 11 about here.]

5. Numerical investigations of correlation length evolutions upon failure

5.1. Influence of the loading type

5.1.1. Response in direct tension

In this subsection, the correlation length extraction method is applied to a direct tension test. We consider a concrete specimen presenting the same characteristics than the one studied in section 4.1.

[Figure 12 about here.]

Figure 12 presents the tension test geometry and the Force vs. CMOD curves. The specimen is pre-notched from the bottom face to half the depth and the test is CMOD controlled. At each CMOD step, the distribution of incremental damage events is plotted (see figure 13.a) and the corresponding Ripley's residual function is estimated. The correlation length is then extracted based on the analysis by Ripley's functions as presented in section 2.3.

This correlation length is directly related to the size of the damage zone and therefore to the internal length in a nonlocal continuum setting. The evolution of the extracted correlation length is presented in figure 13.b. In concrete, damage develops at the interface between aggregates and mortar. At the beginning of the test, damage develops and spreads all over the specimen and then the correlation length grows and it would reach eventually the size of the box. However, at CMOD$\approx$ 0.01 mm, damage starts to localize within a fracture process zone surrounding the pre-notch tip and the correlation length reaches a plateau. Later on, and as the fracture process zone develops to form a macro-crack, the correlation length decreases. When the macro-crack is fully developed, surrounded by the fracture process zone, the correlation length reaches a new plateau at a value corresponding to four times the larger aggregate size ($\approx$ 10 mm).

[Figure 13 about here.]

5.1.2. Response in bending

In this subsection, the correlation length extraction method is applied to the three point bending beams presented in section 4.1. We compare here the response of long notch and unnotched specimens with a depth of 100 mm. Geometries are presented in figure 9. The same post processing method is applied: the test are CMOD controlled and at each CMOD step, the distribution of incremental damage events is plotted (see figure 14.a-b) and the corresponding Ripley's residual function is estimated. The correlation length is extracted based on the analysis by Ripley's functions as presented in section 2.3. The evolution of the extracted correlation length is presented in figure 14.c.

[Figure 14 about here.]

For the notched specimen, the evolution of damage is similar to what has been observed in direct tension. The pre-notch trigs the damage localization and the correlation length grows to reach a plateau at a value corresponding to four/five times the larger aggregate size ($\approx$ 10 mm). However, during the initiation of failure, damage does not spread over the whole specimen because of the bending strain gradient. That is the reason why only a growing phase is observed before the plateau. For the unnotched specimen, the damage evolution is totally different. Since there is no pre-notch, the damage localization is not trigged and damage spreads on the bottom surface of the specimen. Therefore, the correlation length is equal to the analysis box size at the beginning at damage initiation. At some point, a macro-crack will emerges from the bottom face and propagates surrounded by a fracture process zone. The correlation length is decreasing from the analysis box size to reach the same plateau observed for a notched specimen at a value corresponding to four/five times the larger aggregate size ($\approx$ 10 mm).

6. Concluding remarks

We have presented a detailed analysis based on Ripley's functions of the cracking process at the mesoscale of concrete specimen, both numerically and experimentally. The computational model is a lattice-based approach which already proved to be able to capture size effect test data for notched and unnotched bending beams and the force v.s. CMOD response as well (see [12]). Moreover, comparison with experiments coupled with acoustic emission analyses proved also that the mesoscale model is representative of the local process of quasi-brittle failure in term of dissipative energy maps and histograms of relative distances between damage events (see [5]).

The following concluding statements can be made:

- The post processing with Ripley's function provides indicators of the randomness of a distribution of events.
- It has been shown that a correlation length, which may possibly be linked to an internal length in the sense of non local models, may be extracted from the Ripley's function analyse applied to damage mechanics. However, the exact correspondance between the extracted correlation length and a nonlocal model internal length remains to be derived.

- The evolutions of this extracted correlation length upon failure have been presented. Comparisons between numerical data based on mesoscale lattice modeling and experimental data where damage events were localized by acoustic emission techniques were performed. Even if an important scattering is observed on the experimental data, we observed a global good agreement between the experimental and the numerical results. This means that the numerical model and the Ripley's post-processing procedure may be used alone to investigate the evolution of the correlation length upon failure.

- Numerical investigations have been performed on both direct tension and three point bending specimens. The results show that the extracted correlation length is not constant during failure and significant differences may be observed depending on the type of loading applied to the same specimen.

This conclusion opens the path for further analyses of the fracture process, solely based on numerical analyses with the mesoscale model. From theses studies, a better understanding of the correlations between damage events, that should result into non local continuum modeling at the macroscale, is expected.

Acknowledgments

Financial support from TOTAL Exploration & Production under the project "Fracture and permeability of heterogeneous quasi-brittle materials" is gratefully acknowledged. The authors wish also to acknowledge the University of Bordeaux for the use of the cluster AVAKAS.

[1] D. Grégoire, L. B. Rojas-Solano, G. Pijaudier-Cabot, Failure and size effect for notched and unnotched concrete beams, Int. J. Numerical and Analytical Methods in Geomechanics 37 (10) (2013) 1434–1452. doi:10.1002/nag.2180.

[2] S. Granger, A. Loukili, G. Pijaudier-Cabot, G. Chanvillard, Experimental characterization of the self-healing of cracks in an ultra high performance cementitious material: Mechanical tests and acoustic emission analysis, Cement and Concrete Research 37 (4) (2007) 519 – 527. doi:http://dx.doi.org/10.1016/j.cemconres.2006.12.005.

[3] E. N. Landis, Micro-macro fracture relationships and acoustic emissions in concrete, Construction and Building Materials 13 (12) (1999) 65 – 72. doi:http://dx.doi.org/10.1016/S0950-0618(99)00009-4.

[4] K. Otsuka, H. Date, Fracture process zone in concrete tension specimen, Engineering Fracture Mechanics 65 (23) (2000) 111 – 131. doi:http://dx.doi.org/10.1016/S0013-7944(99)00111-3.

[5] Grégoire, D. and Verdon, L. B. and Lefort, V. and Grassl, P. and Saliba, J. and Regoin, J.-P. and Loukili, A. and Pijaudier-Cabot, G., Mesoscale analysis of failure in quasi-brittle materials: comparison between lattice model and acoustic emission data, International Journal of Numerical and Analytical Methods in Geomechanics (2015) doi: 10.1002/nag.2363.

[6] K. Haidar, G. Pijaudier-Cabot, J. Dubé, A. Loukili, Correlation between the internal length, the fracture process zone and size effect in model materials, Materials and Structures 38 (2) (2005) 201–210.

[7] D. Grégoire, L. B. Rojas-Solano, G. Pijaudier-Cabot, Continuum to discontinuum transition during failure in non-local damage models, International Journal for Multiscale Computational Engineering 10 (6) (2012) 136. doi:10.1615/IntJMultCompEng.2012003061.

[8] C. Giry, F. Dufour, J. Mazars, Stress-based nonlocal damage model, International Journal of Solids and Structures 48 (25-26) (2011) 3431–3443.

[9] A. Krayani, G. Pijaudier-Cabot, F. Dufour, Boundary effect on weight function in nonlocal damage model, Engineering Fracture Mechanics 76 (14) (2009) 2217–2231.

[10] K. Duan, X. Hu, F. Wittmann, Boundary effect on concrete fracture and non-constant fracture energy distribution, Engineering Fracture Mechanics 70 (16) (2003) 2257 – 2268, ¡ce:title¿Size-scale effects¡/ce:title¿. doi:http://dx.doi.org/10.1016/S0013-7944(02)00223-0.

[11] C. La Borderie, C. Lawrence, A. Menou, Approche mésoscopique du comportement du béton: Apport de la représentation géométrique, Revue européenne de génie civil 11 (4) (2007) 407–421.

[12] P. Grassl, D. Grégoire, L. B. Rojas-Solano, G. Pijaudier-Cabot, Meso-scale modelling of the size effect on the fracture process zone of concrete, International Journal of Solids and Structures 49 (13) (2012) 1818–1827.

[13] B. . D. . Ripley, Modelling Spatial Patterns, Journal of the Royal Statistical Society. Series B (Methodological) 39 (2) (1977) 172–212.

[14] P. M. Dixon, Ripleys K function, in: A. H. El-shaarawi, W. W. Piegorsch (Eds.), Encyclopedia of Environmetrics, volume 3, Vol. 3, John Wiley & Sons, Ltd., Chichester, 2002, pp. 1796–1803.

[15] R. P. Duncan, Flood Disturbance and the Coexistence of Species in a Lowland Podocarp Forest, South Westland, New Zealand Author(s):, Journal of Ecology 81 (3) (1993) 403–416.

[16] N. E. Stamp, J. R. Lucas, Spatial Patterns and Dispersal Distances of Explosively Dispersing Plants in Florida Sandhill Vegetation, Journal of Ecology 78 (3) (1990) 589–600.

[17] P. J. Diggle, A. G. Chetwynd, Second-Order Analysis of Spatial Clustering for Inhomogeneous Populations, Biometrics 47 (3) (1991) 1155–1163.

[18] A. Tordesillas, S. Pucilowski, L. Sibille, F. Nicot, F. Darve, Multiscale characterisation of diffuse granular failure, Philosophical Magazine 92 (36) (2012) 4547–4587.

[19] F. Goreaud, R. Pélissier, On explicit formulas of edge effect correction for ripley's k-function, Journal of Vegetation Science 10 (3) (1999) 433–438.

[20] W. H. Press, B. P. Flannery, S. A. Teukolsky, W. T. Vetterling, Numerical recipes 3rd edition: The art of scientific computing, Cambridge university press, 2007.

[21] P. Grassl, M. Jirásek, Meso-scale approach to modelling the fracture process zone of concrete subjected to uniaxial tension, International Journal of Solids and Structures 47 (7-8) (2010) 957–968.

[22] P. Grassl, A lattice approach to model flow in cracked concrete, Cement and Concrete Composites 31 (7) (2009) 454 – 460. doi:http://dx.doi.org/10.1016/j.cemconcomp.2009.05.001.

[23] D. Griffiths, M. GGW, Modelling of elastic continua using a grillage of structural elements based on discrete element concepts, International Journal for Numerical Methods in Engineering 50 (2001) 1759–1775.

[24] J. Bolander, S. S, Fracture analysis using spring networks with random geometry, Engineering Fracture Mechanics 61 (1998) 569–591.

[25] T. T. C. HSU, F. O. Slate, Tensile Bond Strength Between Aggregate and Cement Paste or Mortar, ACI Journal Proceedings 60 (4) (1963) 465–486.

[26] J. van Mier, Fracture processes of concrete. Assessment of material for fracture models, CRC Press, Boca Raton, USA, 1997.

[27] S. Alam, S. J, L. A, Fracture examination in concrete through combined digital image correlation and acoustic emission techniques, Construction and Building Materials 69 (2014) 232–242.

List of Figures

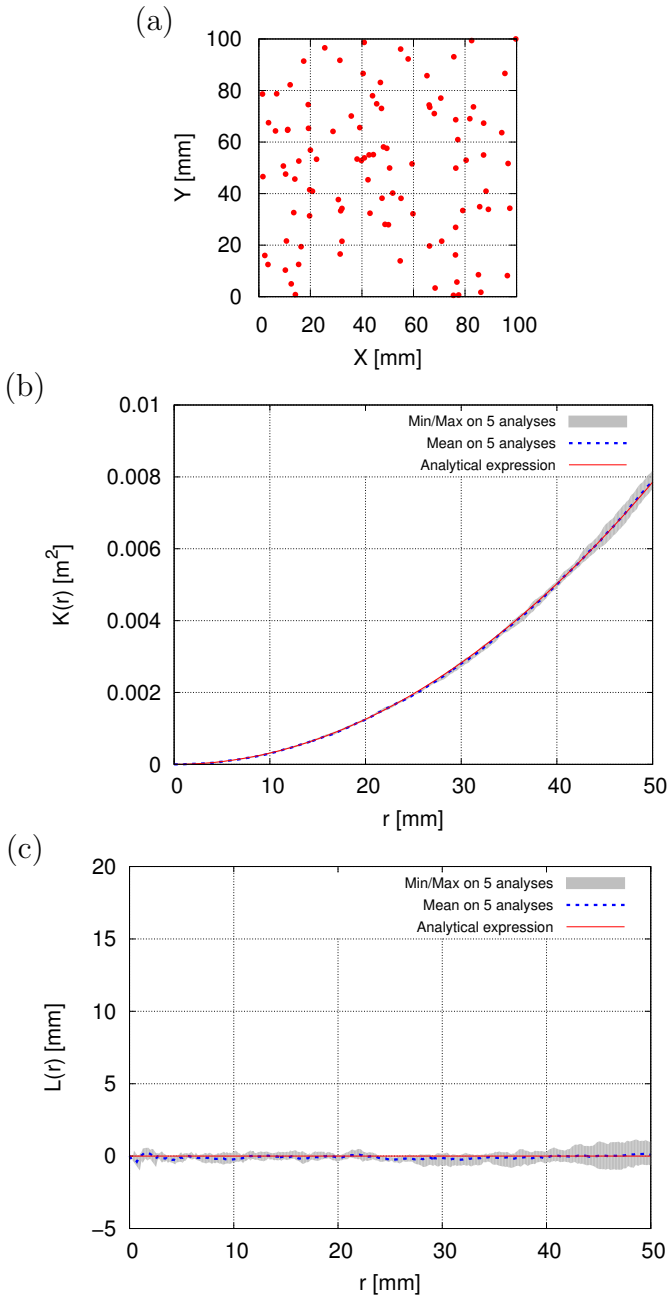

Figure 1: (a) Random distribution of type "A"; (b) K function envelope for the 5 different analyses; (c) L function envelope for the 5 different analyses.

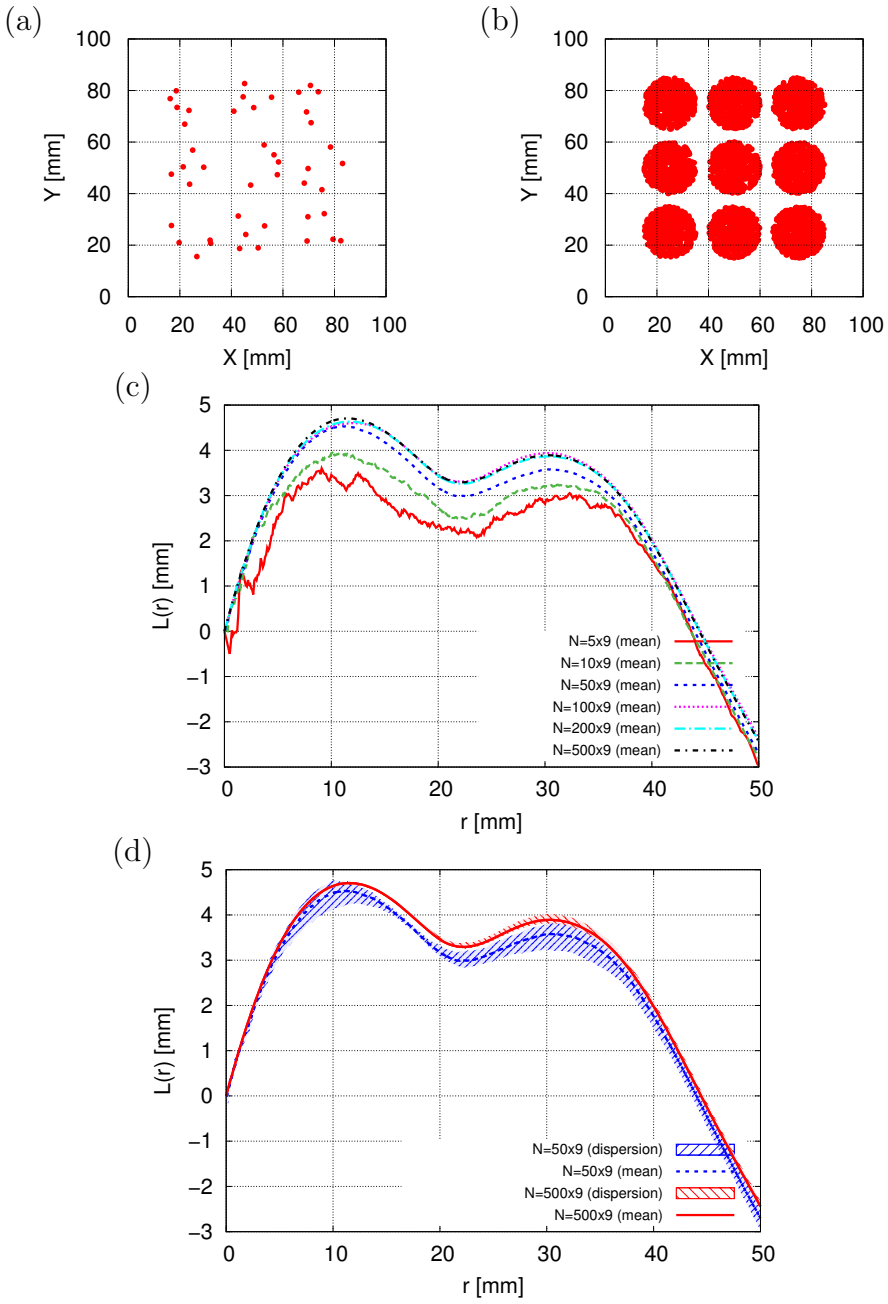

Figure 2: (a) Distribution of type "B" ($N = 5 \times 9$ points); (b) Distribution of type "B" ($N = 500 \times 9$ points); (c)-(d) L function convergence and envelopes for 5 different analyses.

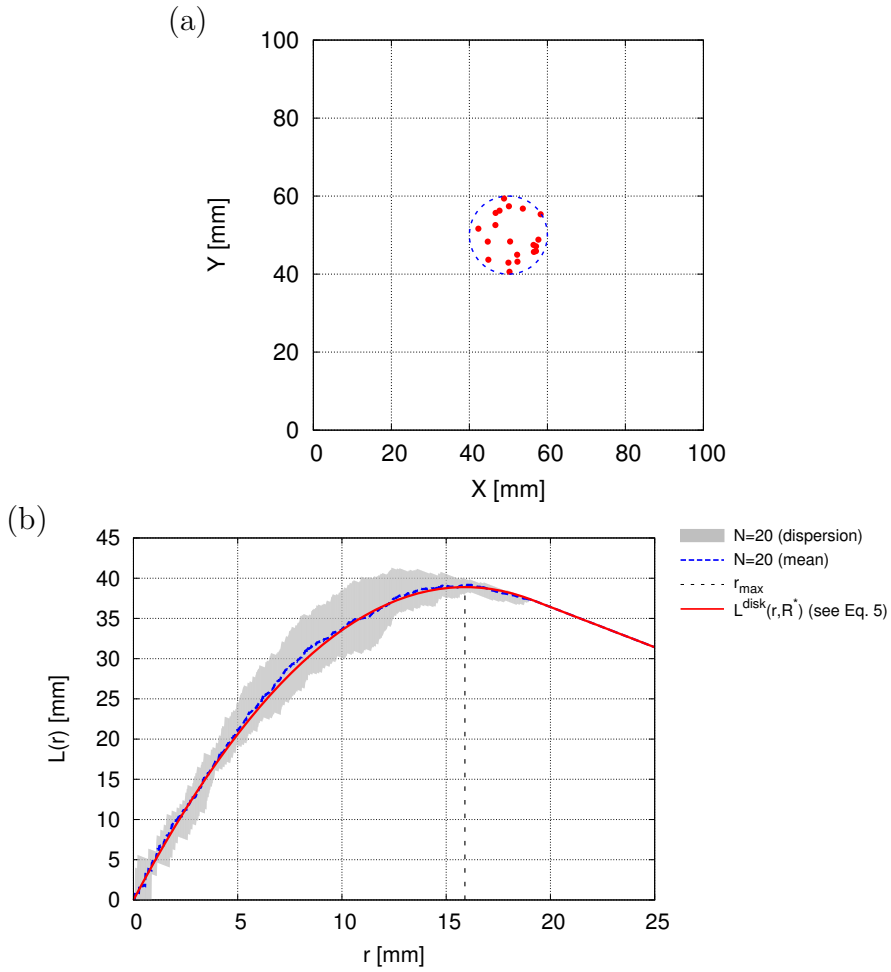

Figure 3: Distribution of events located in a disk of radius $R_0 = 10$ mm (a) and corresponding residual function for 5 different analyses (b).

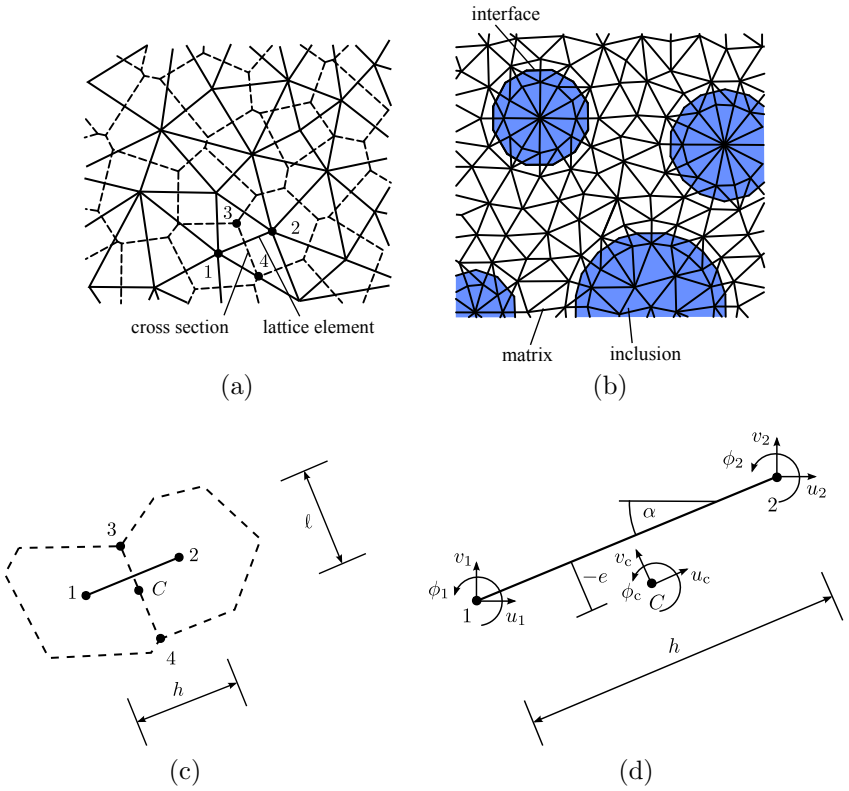

Figure 4: (a) Set of lattice elements (solid lines) with middle cross-sections (dashed lines) obtained from the Voronoi tessellation of the domain. (b) Arrangement of lattice elements around aggregates (inclusions); (c) and (d) Lattice element in the global coordinate system (Reproduced from [12]).

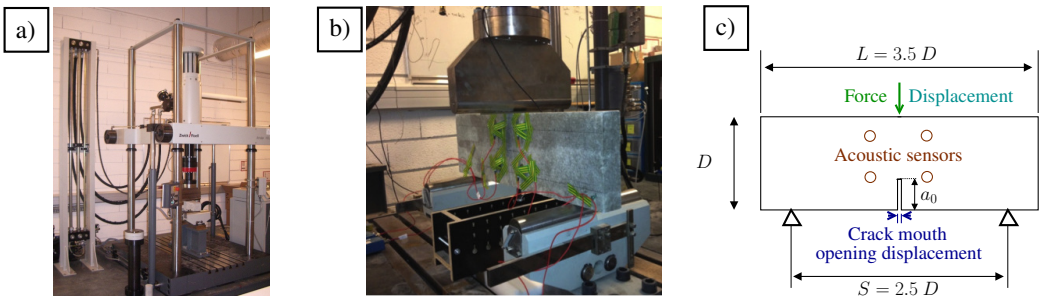

Figure 5: Photography of the servo-hydraulic testing machine (a), zoom on the test rig (b) and sketch of the specimen geometry and measurable quantities (c). Reproduced from [5].

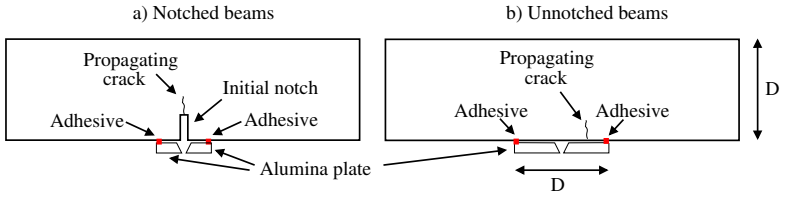

Figure 6: CMOD measurement for (a) notched and (b) unnotched beams (Reproduced from [1]).

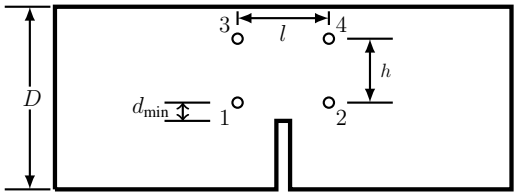

(a) Half-notched beam (HN)

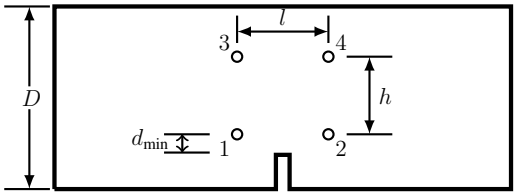

(b) Fifth-Notched beam (FN)

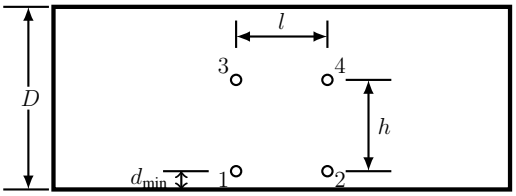

(c) Unnotched beam (UN)

(mm)	HN200	SN200	UN200	UN100
d_{min}	12.5			
l	120			
h	75	105	110	60

Figure 7: Position of the acoustic sensors for the three different beam geometries. Reproduced from [5].

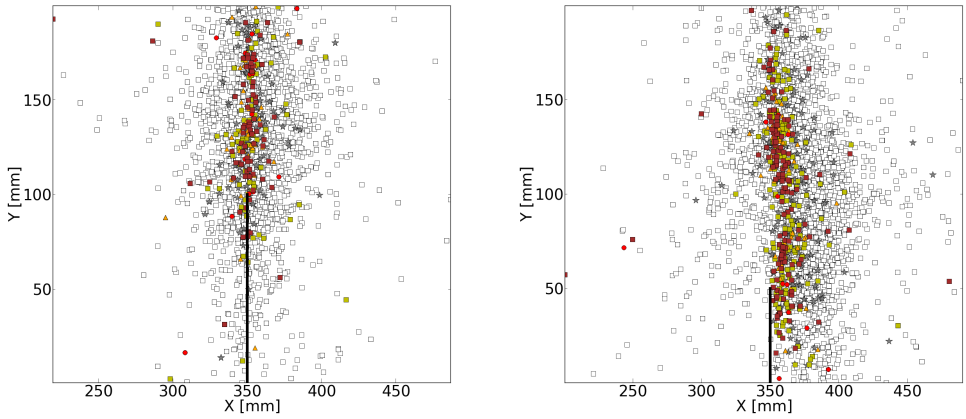

(a) Beam 1125 – $D = 200$ mm, $a_0 = 0.5$(b) Beam 1121 – $D = 200$ mm, $a_0 = 0.2$

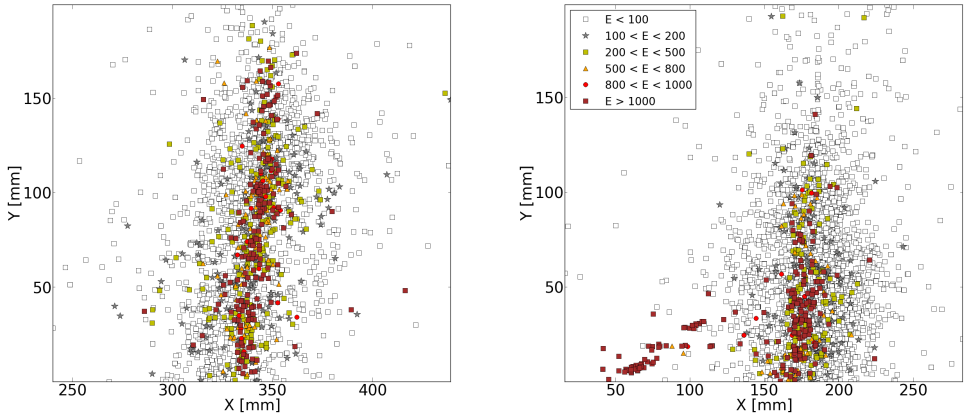

(c) Beam 1122 – $D = 200$ mm, $a_0 = 0$ (d) Beam 1131 – $D = 100$ mm, $a_0 = 0$

Figure 8: Distribution of acoustic events in different geometries of beam – map of distribution of energies. Reproduced from [5].

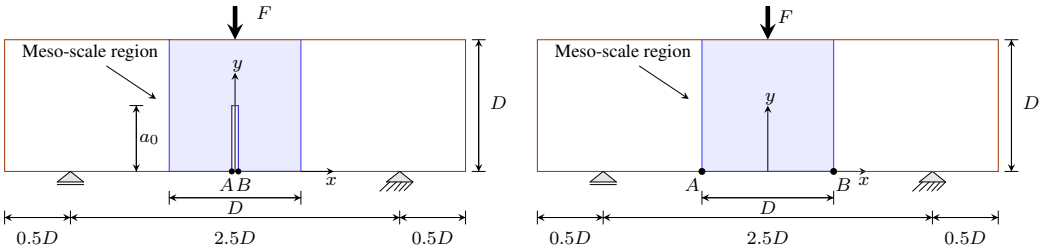

(a) Half-Notched beam (b) Unnotched beam

Figure 9: Geometries of three-point bending test for (a) notched and (b) unnotched beams.

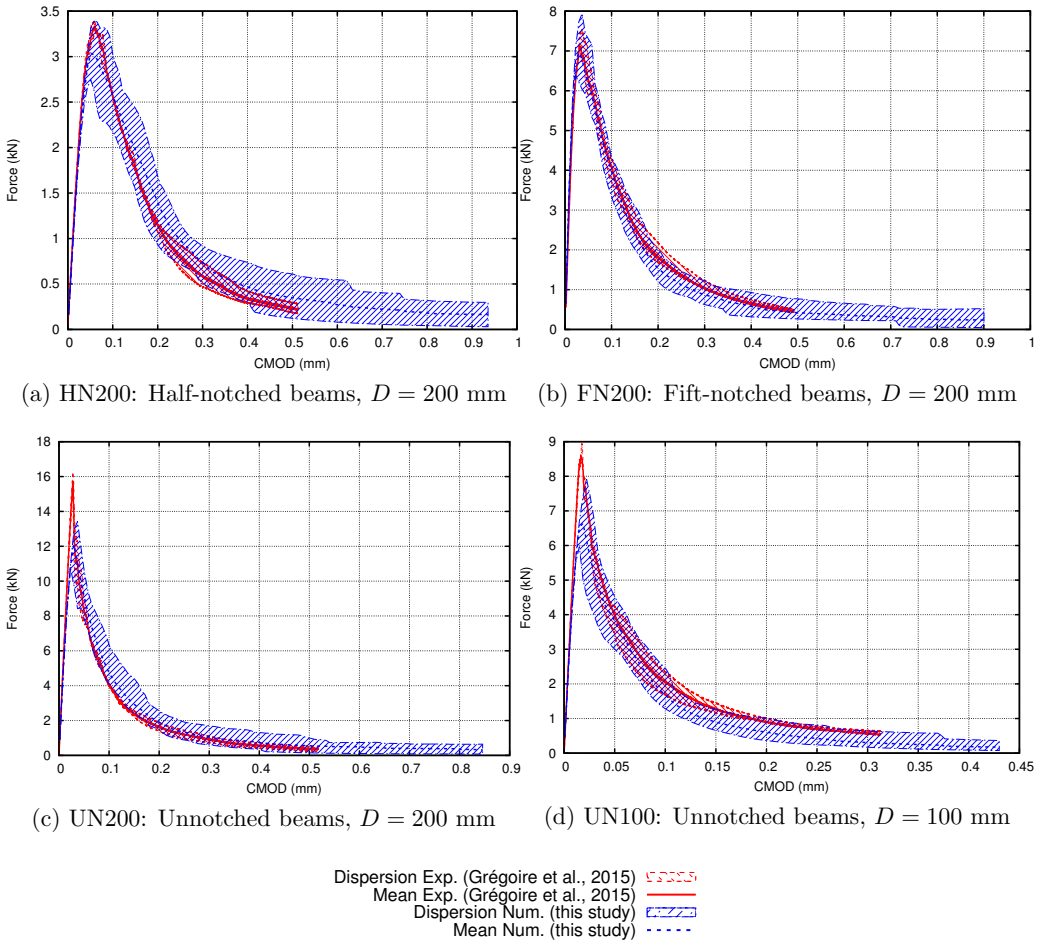

(a) HN200: Half-notched beams, $D = 200$ mm (b) FN200: Fift-notched beams, $D = 200$ mm

(c) UN200: Unnotched beams, $D = 200$ mm (d) UN100: Unnotched beams, $D = 100$ mm

Figure 10: Force vs. CMOD raw curves.

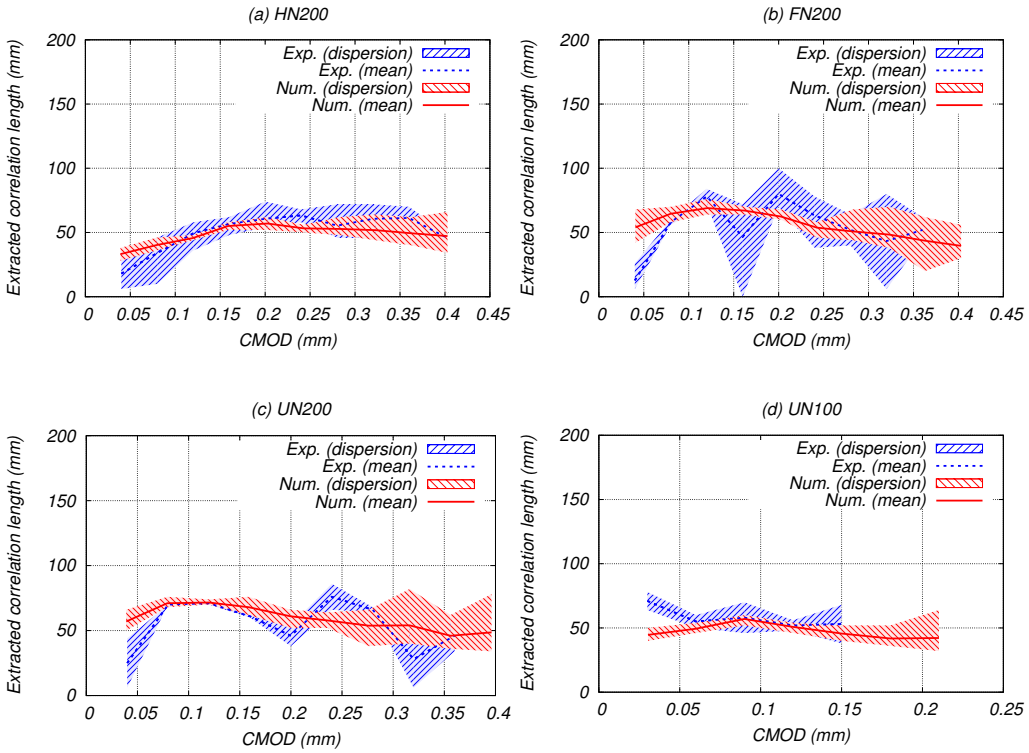

Figure 11: Comparison between experimental and numerical extracted correlation length with intensity conversion (geometry labels refer to table 3).

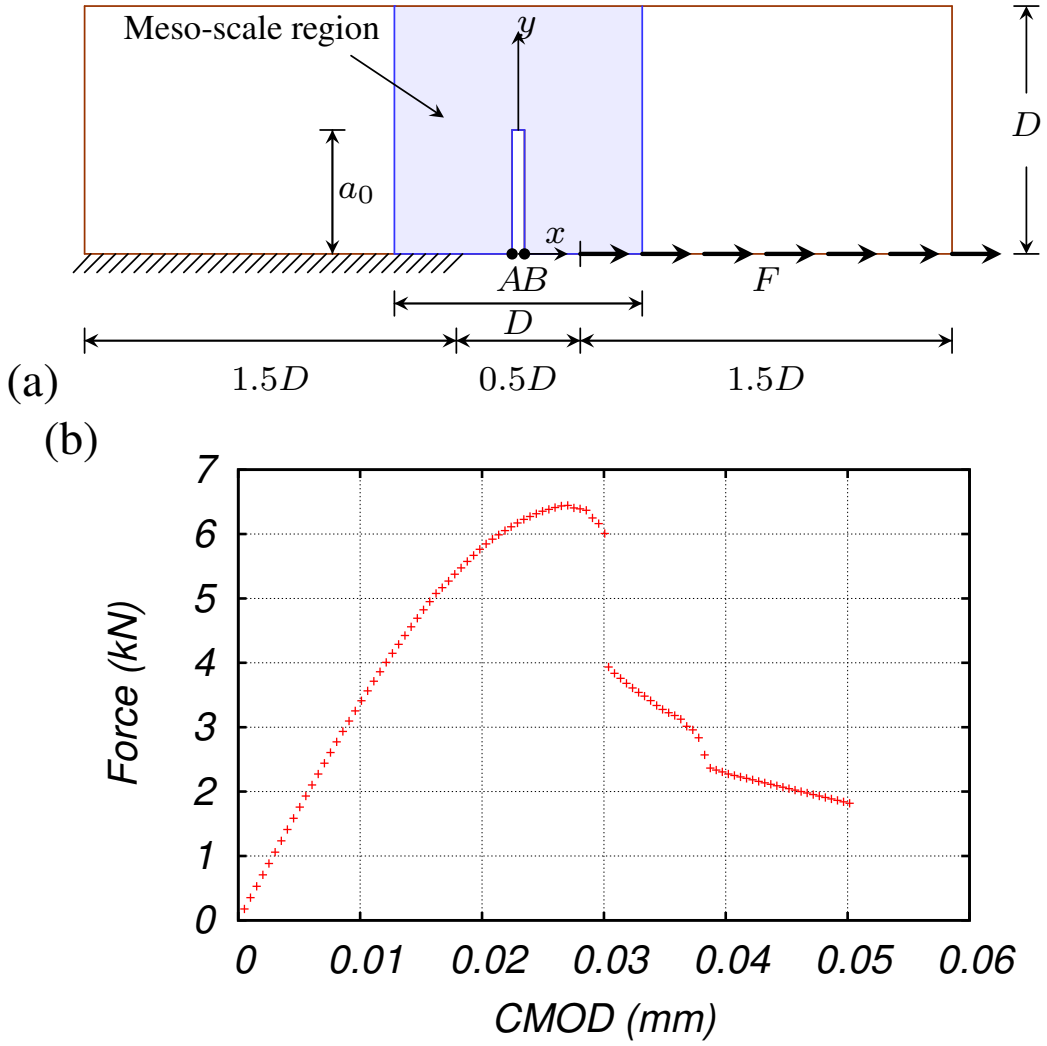

Figure 12: (a) Geometry and (b) Force vs. CMOD curves of the direct tension test ($D = 100$ m).

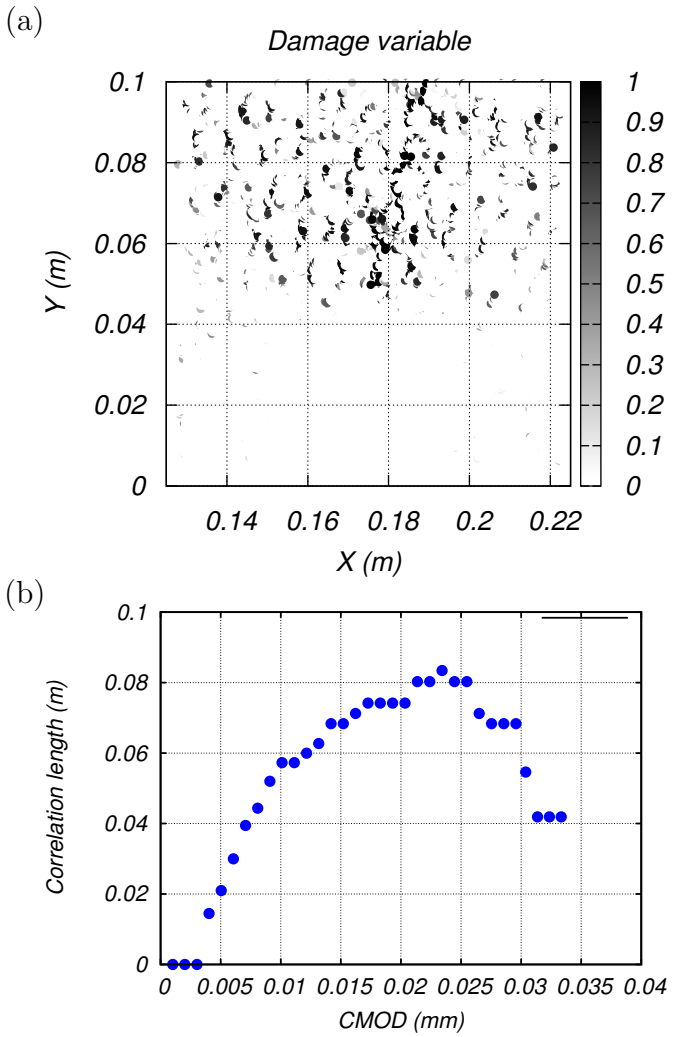

Figure 13: Distribution of damage events for a direct tension test (a) and corresponding correlation length evolution (b).

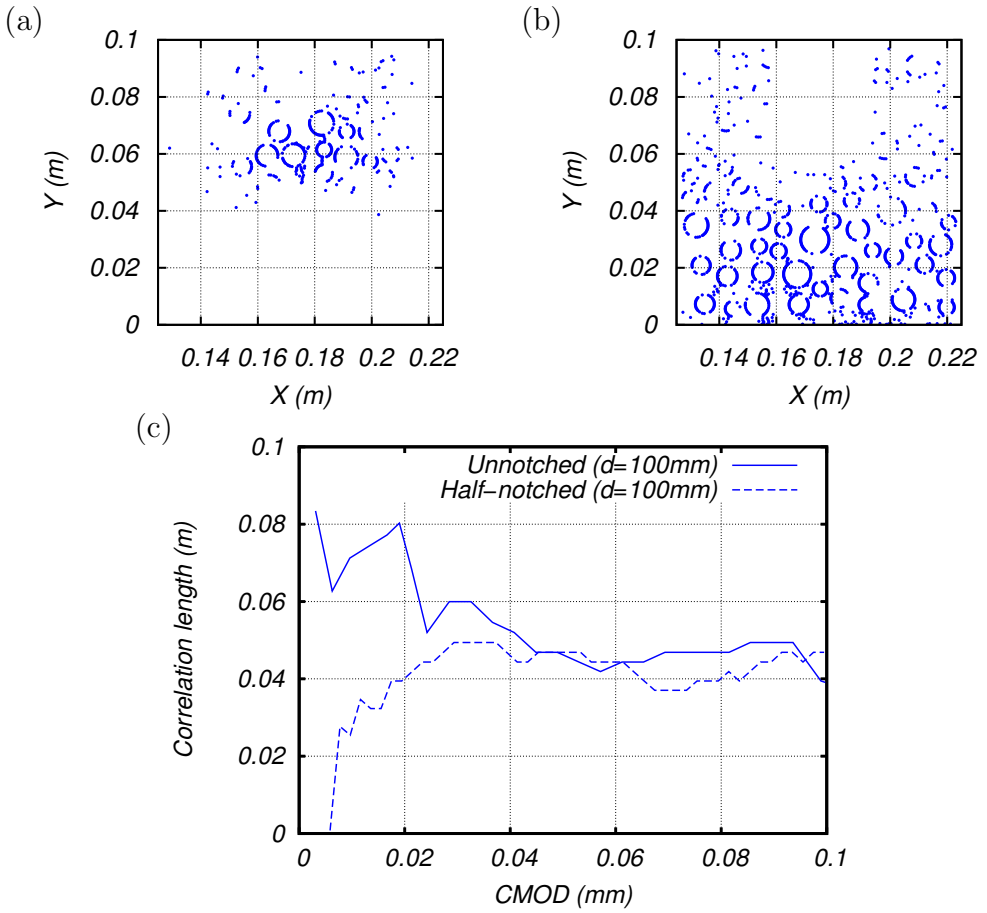

Figure 14: Responses in bending: (a) Damage distribution at peak for the long notch specimen; (b) Damage distribution at peak for the unnotched specimen; (c) Evolution of the extracted correlation lengths for both specimen.

List of Tables

Product	Designation	Mass (kg)
Sand	Cemex 0/4	740
Aggregates	Durruty 4/10	1140
Cement	Calcia CEM II/A	286
Admixture	Axim Cimplast 115	1
Water	Clarified water	179
	Total	2346

Table 1: Concrete mixture formulation.

Compressive strength			Young modulus			Poisson ratio			Tensile strength		
μ	σ	c_v	μ	σ	c_v	μ	σ	c_v	μ	σ	c_v
(MPa)	(MPa)	(%)	(GPa)	(GPa)	(%)	(–)	(–)	(%)	(MPa)	(MPa)	(%)
42.3	2.8	6.6	37.0	0.9	2.4	0.21	0.02	8.7	3.9	0.2	6.0

(μ – mean value; σ – standard deviation; $c_v = \mu/\sigma$ – coefficient of variation)

Table 2: Concrete mean mechanical properties.

Label	D (mm)	a_0 (mm)	v_{CMOD} (μm/s)
HN200	200	100	0.3
FN200	200	40	0.3
UN200	200	0	0.3
UN100	100	0	0.2

Table 3: Specimen dimensions and experimental conditions.

Table 4: Model parameters.

	E [GPa]	ν	f_t [MPa]	q	c	G_f [N/m]
Matrix	44	0.33	3.8	2	10	86
Interface	58.7	0.33	1.9	2	10	43
Aggregate	88	0.33	-	-	-	
Mean	63	0.33	-	-	-	